



MOX-Report No. 35/2020

**Wall shear stress topological skeleton independently
predicts long-term restenosis after carotid bifurcation
endarterectomy**

Morbiducci, U.; Mazzi, V.; Domanin, M.; De Nisco, G.;
Vergara, C.; Steinman, D.A.; Gallo, D.

MOX, Dipartimento di Matematica
Politecnico di Milano, Via Bonardi 9 - 20133 Milano (Italy)

mox-dmat@polimi.it

<http://mox.polimi.it>

WALL SHEAR STRESS TOPOLOGICAL SKELETON INDEPENDENTLY PREDICTS LONG-TERM RESTENOSIS AFTER CAROTID BIFURCATION ENDARTERECTOMY

Umberto Morbiducci ^{a*}, Valentina Mazzi ^{a*}, Maurizio Domanin ^{b-c}, Giuseppe De Nisco ^a,
Christian Vergara ^d, David A. Steinman^e, Diego Gallo ^{a†}

^a Polito^{BIO}Med Lab, Department of Mechanical and Aerospace Engineering, Politecnico di Torino, Turin, Italy

^b Department of Clinical Sciences and Community Health, Università di Milano, Italy

^c Unità Operativa di Chirurgia Vascolare, Fondazione I.R.C.C.S. Cà Granda Ospedale Maggiore Policlinico, Milano, Italy

^d Laboratory of Biological Structure Mechanics (LaBS), Dipartimento di Chimica, Materiali e Ingegneria Chimica “Giulio Natta”, Politecnico di Milano, Italy

^e Biomedical Simulation Laboratory, Department of Mechanical & Industrial Engineering, University of Toronto, Toronto, ON Canada

* The authors equally contributed to this study

Abbreviated title: WSS topological skeleton predicts restenosis after CEA

† Address for correspondence:

Diego Gallo, PhD

Polito^{BIO}Med Lab, Department of Mechanical and Aerospace Engineering

Corso Duca degli Abruzzi, 24 – 10129 Turin, Italy

Tel: +39 011 090 6574

Fax: +39 011 090 6999

Email: diego.gallo@polito.it

ABSTRACT

Wall shear stress (WSS) topological skeleton, composed by fixed points and the manifolds linking them, reflects the presence of blood flow features associated to adverse vascular response. However, the influence of WSS topological skeleton on vascular pathophysiology is still underexplored. This study aimed to identify direct associations between the WSS topological skeleton and markers of vascular disease from real-world clinical longitudinal data of long-term restenosis after carotid endarterectomy (CEA).

Personalized computational hemodynamic simulations were performed on a cohort of 13 carotid models pre-CEA and at 1 month after CEA. At 60 months after CEA, intima-media thickness (IMT) was measured to detect long-term restenosis. The analysis of the WSS topological skeleton was carried out by applying a Eulerian method based on the WSS vector field divergence. To provide objective thresholds for WSS topological skeleton quantitative analysis, a computational hemodynamic dataset of 46 ostensibly healthy carotid bifurcation models was considered.

CEA interventions did not completely restore physiological WSS topological skeleton features. Significant associations emerged between IMT at 60 months follow-up and the exposure to (1) high temporal variation of WSS contraction/expansion ($R^2=0.51$, $p<0.05$), and (2) high fixed point residence times, weighted by WSS contraction/expansion strength ($R^2=0.53$, $p<0.05$). These WSS topological skeleton features were statistically independent from the exposure to low WSS, a previously reported predictor of long-term restenosis, therefore representing different hemodynamic stimuli and potentially impacting differently the vascular response. This study confirms the direct association between WSS topological skeleton and vascular response, contributing to elucidate the mechanistic link between flow disturbances and clinical observations of vascular lesions.

Keywords: Fixed points; manifolds; wall shear stress divergence; computational fluid dynamics; intima-media thickness.

LIST OF ABBREVIATIONS

CB = carotid bulb

CCA = common carotid artery

CEA = carotid endarterectomy

DUS = Doppler ultrasound

ECA = external carotid artery

ICA = internal carotid artery

IMT = intima-media thickness

LSA = low shear area

MRA = magnetic resonance angiography

PSV = peak systolic velocity

TAWSS = time-averaged wall shear stress

TSVA = topological shear variation area

TSVI = topological shear variation index

wFPA = weighted fixed point area

WSS = wall shear stress

INTRODUCTION

Extensive research has investigated the mechanisms through which the hemodynamic environment at the carotid artery bifurcation influences the origin and progression of cardiovascular diseases.²⁶ In particular, wall shear stress (WSS) has been recognized as atherogenic,²⁶ with previous evidence demonstrating that exposure to low¹⁴ and oscillatory¹⁹ WSS is a significant independent risk factor for identifying individuals at greater susceptibility for carotid atherosclerosis. The exposure to low WSS appears promising also in terms of predicting the risk of long-term restenosis after carotid endarterectomy (CEA), a surgical intervention consisting in the removal of the plaque on both symptomatic and asymptomatic patients with moderate to severe carotid stenosis.²⁷ Long-term restenosis, an important complication affecting CEA outcome leading to development of cerebral symptoms or even carotid occlusion and stroke, presents similarities with native carotid artery stenosis^{18,27} when the absence of post-CEA residual atherosclerosis and short-term restenosis (i.e. <24 months^{13,18}) are accounted for. Thus, the mechanisms underlying both atherosclerosis and long-term restenosis are mechanistically influenced by the hemodynamic environment. However, the specificity of the currently considered hemodynamic features and their clinical added value, hampered by the practical challenges of carrying out large prospective clinical studies, have been questioned.²⁸

To improve, refine and extend our current understanding of the association between local hemodynamics and vascular disease, an increasing interest has been recently dedicated to the analysis of WSS vector field topological skeleton,^{5,6,24} composed by fixed points and the stable/unstable manifolds connecting them. At a fixed point, the WSS vector field focally vanishes, and manifolds identify regions where the WSS vector field exerts a contraction/expansion action on the endothelial

cells at the luminal surface.²⁴ It can therefore be presumed that the WSS topological skeleton features influence vascular pathophysiology. This presumption is supported by the fact that the WSS topological skeleton is determined by blood flow structures associated to adverse vascular response at the carotid bifurcation,²⁴ including near-wall flow stagnation, separation and recirculation.⁶ Moreover, the fluid-phase mass transport of solutes near the wall has been demonstrated to be governed by the cycle-average WSS topological skeleton.^{3,6,12} However, the exact mechanisms by which the WSS topological skeleton and related descriptors influence vascular pathophysiology are still underexplored.

The present study investigates the association between the WSS topological skeleton and markers of vascular disease at the carotid bifurcation from real-world, longitudinal clinical data. To do that, a cohort of 12 asymptomatic patients submitted to 13 CEA interventions¹⁰ was adopted. A recently proposed Eulerian-based analysis²⁴ of the topological skeleton of the WSS vector field was applied to patient-specific computational hemodynamic models of the carotid bifurcation at 1 month after CEA. Intima-media thickness (IMT) was clinically measured at 60 months after CEA to provide an indicator of vascular response and detect the presence of long-term restenosis. Additionally, to explore how the CEA intervention impacts local hemodynamics and, ultimately, the clinical outcome, the WSS topological skeleton analysis was carried out on the pre-CEA (i.e., stenotic) carotid bifurcation models. For the purpose of contextualization of the results, the WSS topological skeleton analysis was (1) extended to a computational hemodynamics dataset of 46 ostensibly healthy carotid bifurcation models, and (2) complemented with the analysis of the exposure to low WSS, which was previously demonstrated to be directly associated to adverse vascular responses on the same post-CEA dataset adopted here.¹⁰

METHODS

Patient population data

Thirteen carotid endarterectomy procedures were performed in twelve real world patients with diameter stenosis of greater than 70% at the Vascular Surgery Operative Unit of Fondazione IRCSS Ca' Granda, Ospedale Maggiore Policlinico in Milan. As detailed elsewhere,^{8,9} all cases were asymptomatic, one case had contralateral occlusion of the internal carotid artery (ICA), and three cases were previously submitted to contralateral CEA. Age, sex, location of carotid stenosis, diameters of ICA and risk factors are listed in Table 1. The study was approved by the I.R.C.C.S. Fondazione Policlinico Ethics Committee according to institutional ethics guidelines, and participants provided informed consent.

Patch graft angioplasty was performed in 9 cases (PG1-9) using a polyester collagen-coated patch (Ultra-thin Intervascular[®], Mahwah, NJ U.S.A), and 4 cases underwent primary closure, i.e. without patch graft (PC1-4). Further details about the surgical cohort are reported elsewhere.^{10,17}

All patients were then submitted to Doppler ultrasound (DUS) follow-up at 3, 24 and 60 months. Cases of restenosis were defined by a peak systolic velocity (PSV) of >130 cm/s as measured by DUS (an indicator of the presence of a diameter stenosis greater than 50%,¹ according to the European Carotid Stenosis Trial standard). No sign of restenosis and no symptoms of cerebrovascular ischemia emerged in any patient from follow-ups at 3 and 24 months. During the follow-up period, one patient died for myocardial infarction (PG4), and one for pancreatic carcinoma (PG8). All eligible patients were submitted to DUS follow-up at 60 months. Intima-media thickness (IMT) was measured using a Philips iU22 ultrasound scanner with linear 8 MHz probe (Philips Ultrasound, Bothwell, U.S.A) and automatically extracted offline with the clinical software Qlab (Philips Ultrasound, Bothwell, U.S.A) at

the following locations: ICA distal to the carotid bulb (CB); CB; distal end of the common carotid artery (CCA), i.e., the flow divider (FD); CCA at 1 cm and 2 cm from the distal end of the CCA (FD-1cm and FD-2cm, respectively). For the sake of synthesis and as previously proposed,¹⁰ the maximum IMT found in the bifurcation region was also considered.

Computational Hemodynamics

Pre-CEA and post-CEA cohorts

Magnetic resonance angiography (MRA) acquisitions were performed before and within a month after surgery to obtain the pre-CEA and post-CEA 3D geometry of the carotid bifurcations, as detailed elsewhere.^{10,17}

Blood was modelled as an incompressible homogeneous Newtonian fluid,^{22,25} under laminar flow and rigid wall assumptions.^{9,17} The governing equations of fluid motion were solved numerically using the finite-element library LifeV (<http://www.lifev.org>) in discretized fluid domains with tetrahedral meshes¹⁷. Patient-specific flow rate waveforms were extracted before and after CEA from echo-color DUS at the CCA and ICA, and imposed as boundary conditions in the numerical simulations. At the external carotid artery (ECA) outlet section, a traction-free condition was imposed to ensure instantaneous mass conservation. Details on image acquisition and computational settings are extensively described elsewhere.^{9,10,17}

Healthy cohort

To characterize the WSS topological skeleton features of the physiological carotid artery hemodynamics, and provide objective thresholds for quantitative analysis of the WSS topological

skeleton descriptors introduced in the following, the topological skeleton analysis was performed on a previously characterized computational hemodynamics dataset of 46 ostensibly healthy carotid bifurcation models,^{14,15} denoted with the prefix He (He1-He46). Briefly, the 3D geometry of 46 carotid bifurcations was reconstructed from contrast enhanced MRA²⁹ and the governing equations of fluid motion were solved numerically using a validated in-house finite element solver¹⁴ with the same assumptions as the CEA dataset. Patient-specific flow rate waveforms were extracted from cine phase contrast magnetic resonance acquisitions at the CCA and ICA and imposed as boundary conditions in the numerical simulations, while at the ECA outlet section a traction-free condition was imposed.¹⁴ Further information on computational hemodynamic simulation of the ostensibly healthy carotid bifurcations is detailed elsewhere.^{14,15,29}

WSS Topological Skeleton analysis & quantitative description

Starting from the WSS vector distribution at the luminal surface, the WSS topological skeleton analysis was carried out applying a recently proposed Eulerian method.²⁴ Based on dynamical systems theory, the topological skeleton of the WSS field is composed by fixed points, i.e. points where the WSS vanishes, and manifolds, which identify WSS contraction/expansion regions (attracting/repelling manifolds, respectively) and connect the fixed points. An explanatory sketch of the WSS topological skeleton is presented in Figure 1.

As previously reported, the method applied here rests on the volume contraction theory and analyzes the WSS topological skeleton through the WSS vector field divergence and Poincaré index.²⁴ In

particular it was demonstrated that the WSS manifolds, and hence the connections between WSS fixed points, can be encased by the divergence of the normalized WSS vector field:²⁴

$$\text{DIV}_W = \nabla \cdot \boldsymbol{\tau}_u = \nabla \cdot \left(\frac{\boldsymbol{\tau}}{|\boldsymbol{\tau}|} \right), \quad (1)$$

where $\boldsymbol{\tau}$ is the WSS vector and $\boldsymbol{\tau}_u$ is its normalized (i.e., unit) version. More in detail, the divergence of the normalized WSS vector field can be used to localize and identify the WSS spatial contraction/expansion configuration patterns at the carotid luminal surface with negative/positive values of DIV_W , respectively (Figure 1).²⁴ To obtain the complete WSS topological skeleton, the WSS fixed points locations were determined using the Poincaré index.²⁴ Then, the identified fixed points were classified according to their nature (saddle point, node or focus, Figure 1), using the largely adopted approach based on the eigenvalues of the Jacobian matrix of the WSS vector field,¹⁶ $\lambda_1, \lambda_2, \lambda_3$ (with $\sum_{i=1}^3 \lambda_i = \nabla \cdot \boldsymbol{\tau}$). In detail, as summarized in Figure 1, three real eigenvalues with different signs identify a saddle point. Three real eigenvalues with the same sign identify a node, whose nature is characterized as attracting or repelling (i.e., stable or unstable, respectively)¹⁶ according to their sign (negative or positive, respectively, Figure 1). Complex conjugate eigenvalues identify a stable or unstable focus, according to the sign of the real part (negative or positive, respectively, Figure 1).

As a first step, the WSS topological skeleton of the cycle-average WSS vector field $\bar{\boldsymbol{\tau}}$ at the luminal surface was analyzed. Subsequently, the WSS topological skeleton dynamics along the cardiac cycle was characterized. In order to measure the amount of variation in the WSS contraction/expansion action exerted at the carotid luminal surface along the cardiac cycle, here we adopted the quantity Topological Shear Variation Index (*TSVI*), defined as the root mean square deviation of the divergence of the normalized WSS with respect to its average over the cardiac cycle:

$$TSVI = \left\{ \frac{1}{T} \int_0^T [\text{DIV}_W - \overline{\text{DIV}_W}]^2 dt \right\}^{1/2} = \left\{ \frac{1}{T} \int_0^T [\nabla \cdot (\boldsymbol{\tau}_u) - \overline{\nabla \cdot (\boldsymbol{\tau}_u)}]^2 dt \right\}^{1/2}, \quad (2)$$

where T is the cardiac cycle duration and the overbar denotes a cycle-average quantity.

The unsteady nature of the WSS vector field fixed points along the cardiac cycle was characterized using the WSS fixed point weighted residence time along the cardiac cycle, as recently proposed:²⁴

$$RT\overline{\nabla}_{x_{fp}}(e) = \frac{A_{avg}}{A_e} \frac{1}{T} \int_0^T \mathbb{I}_e(\mathbf{x}_{fp}, t) |(\nabla \cdot \boldsymbol{\tau})_e| dt, \quad (3)$$

where $\mathbf{x}_{fp}(t)$ is the location of a WSS fixed point at time $t \in [0, T]$, e is the generic triangular element of the superficial mesh of area A_e and A_{avg} is the average surface area of all triangular elements of the superficial mesh of the luminal surface of the vessel, \mathbb{I} is the indicator function and $(\nabla \cdot \boldsymbol{\tau})_e$ is the instantaneous WSS divergence value. Using Eq. (3) it is possible to quantify the fraction of cardiac cycle a triangle mesh surface element e on the carotid luminal surface hosted a fixed point, weighting the residence time by the strength of the local contraction/expansion action as measured by the WSS divergence around the fixed point²⁴.

In order to perform a quantitative analysis of the WSS topological skeleton, each pre-CEA, post-CEA and healthy carotid bifurcation was split in its CCA, ICA and ECA branches.² The bifurcation region was delimited by sections located at 3, 5 and 2 radii along the CCA, ICA and ECA, respectively²¹ (denoted CCA3, ICA5 and ECA2). According to a previously employed threshold-based approach for the identification of regions at the luminal surface exposed to disturbed shear,^{10,15,22} here the exposure to large variations in the WSS contraction/expansion action was quantified by the relative surface area exposed to high values of $TSVI$, considering as threshold value the 80th percentile of the pooled $TSVI$ distribution of the healthy models in the CCA3-ICA5-ECA2 region. This variable, denoted as Topological

Shear Variation Area (TSVA), defines the relative area exposed to high normalized WSS divergence variability. Similarly, the exposure to the action of instantaneous WSS fixed points was quantified by the relative surface area exposed to non-null values of $RT\nabla_{x_{fp}}(e)$, i.e. considering the luminal surface area where fixed points occurred along the cardiac cycle in the CCA3-ICA5-ECA2 region. This variable is denoted as weighted Fixed Points Area (wFPA).

To complement the WSS topological skeleton characterization, the luminal distribution of time-averaged wall shear stress (TAWSS) magnitude along the cardiac cycle was also evaluated, as the exposure to low TAWSS values was previously linked to an increased long-term restenosis risk.¹⁰ The exposure to low TAWSS values was quantified by the relative surface area exposed to TAWSS values below a threshold value, corresponding to the 20th percentile of the pooled TAWSS distribution of the healthy models in the CCA3-ICA5-ECA2 region. This variable is denoted as Low Shear Area (LSA).

Statistical analysis

Differences among the three cohorts (i.e., pre-CEA, post-CEA and healthy) in terms of WSS features were evaluated with a Wilcoxon signed-rank test, with significance assumed for $p < 0.05$. The relationships between the relative exposure to high $TSVI$, $RT\nabla_{x_{fp}}(e)$ and low TAWSS (respectively, TSVA, wFPA and LSA) were assessed with linear regression analysis. The quality of the regression was evaluated with the coefficient of determination R^2 . Significance was assumed for $p < 0.05$.

Successively, the nature of the relationship (if any) between WSS topological skeleton descriptors and clinical follow-up data was explored in the post-CEA dataset to test the physiological significance of WSS topological skeleton. Linear regression analysis was used to identify relationships between WSS

topological skeleton descriptors with the measured IMT values. The quality of the regression was evaluated with the coefficient of determination R^2 . Significance was assumed for $p < 0.05$.

RESULTS

Cycle-average WSS vector field topological skeleton analysis

As a preliminary step, an exploration of the cycle-average WSS vector field ($\bar{\tau}$) topological skeleton was carried out to identify its main integral features on pre-CEA, post-CEA and healthy cohorts. Cycle-average WSS contraction/expansion regions, highlighted by the divergence of the normalized cycle-average WSS vector field, are presented in Figure 2. In pre-CEA models, a WSS contraction region was located in correspondence of the cross-sectional area reduction at the stenosis, while for the post-CEA and healthy cohorts contraction and expansion regions were mainly located at the carotid bulb (Figure 2), consistently with previous observations.²⁴ A WSS expansion region was identified around the bifurcation apex as a feature common to all the carotid models (Figure 2). As for the cycle-average WSS fixed points, the analysis highlighted that saddle points, stable foci and unstable nodes were present on the carotid luminal surface of most of the carotid models, independent of the cohort, but at different locations: (1) in the pre-CEA cohort, cycle-average WSS fixed points were mostly located in proximity to the stenosis; (2) on post-CEA models, cycle-average WSS fixed points were located at the carotid bulb, in general with similarities to the cycle-average WSS topological skeleton of healthy carotid bifurcations (Figure 2). A detailed analysis on the occurrence of cycle-average WSS fixed points for pre-CEA, post-CEA and healthy cohorts is reported in the Supplementary Material, highlighting that

the healthy cohort presented on average the largest number of saddle points and unstable nodes in the bifurcation region (Figure S1, Supplementary Material).

WSS topological skeleton dynamics along the cardiac cycle

WSS topological skeleton was then analyzed along the cardiac cycle to account for its dynamics.²⁴ The visualization of the *TSVI* luminal distributions in the pre-CEA and post-CEA cohorts (Figure 3) was extended beyond the bifurcation region delimited by sections CCA3-ICA5-ECA2 to include in the pre-CEA models possible distal ICA/ECA stenoses. For the pre-CEA cohort, *TSVI* maps highlighted that the highest variations in the contraction/expansion action exerted by the WSS on the endothelium along the cardiac cycle were located mainly immediately downstream of the stenosis, where recirculating flow is expected. In the post-CEA cohort, high *TSVI* regions were observed at the cross-sectional enlargement in correspondence of the bifurcation, a known promoter of disturbed flow,^{7,10} and extended downstream in the ICA and ECA. Considering the *TSVI* luminal distributions in the healthy cohort (Figure 3), the regions undergoing large variation in the WSS contraction/expansion action were in general located at the cross-sectional enlargement in the CCA, at the bulb in the ICA and around the bifurcation apex. For each investigated carotid model, the probability density function of *TSVI* is presented in the Supplementary Material (Figure S2), highlighting that low *TSVI* values are associated with the highest probability for all three cohorts (right skewed distributions). The extension of those high *TSVI* regions presented large interindividual variability (Figure 3 and *TSVA* maps in Figure S3, Supplementary Material).

In terms of $TSVI$ averaged over the bifurcation region, marked differences in the distributions as well as significant differences emerged between the healthy and both pre- and post-CEA cohorts ($p < 0.001$), as highlighted by the violin plots in Figure 4. To further characterize the high variations in the contraction/expansion action exerted by the WSS on the endothelium along the cardiac cycle, $TSVA$ values were also evaluated in the three cohorts: (1) markedly different distributions were observed among the three cohorts (Figure 4); (2) statistically significant differences emerged between post-CEA and healthy cohorts for $TSVA$ values ($p < 0.05$, Figure 4); (3) the post-CEA cohort exhibited the lowest intra-variability with respect to the other cohorts for both. mean $TSVI$ and $TSVA$ (Figure 4).

The analysis of the luminal surface distribution of WSS fixed points weighted residence time along the cardiac cycle highlighted their focal nature on the luminal surface of the carotid bifurcations, giving origin to a scattered distribution of non-null $RT\bar{\nabla}_{x_{fp}}$ values (Figure 5). In pre-CEA carotid models, for which the entire reconstructed geometry is presented in Figure 5 to include possible distal ICA/ECA stenoses, the highest $RT\bar{\nabla}_{x_{fp}}$ values were located immediately downstream of the stenosis, differing from the carotid models in the post-CEA and healthy cohorts, the latter exhibiting the lowest $RT\bar{\nabla}_{x_{fp}}$ values. Moreover, a marked co-localization can be observed between high $TSVI$ and high $RT\bar{\nabla}_{x_{fp}}$ regions at the luminal surface (Figures 3 and 5, respectively).

Considering the values of $RT\bar{\nabla}_{x_{fp}}$ averaged over the bifurcation region, also in this case marked differences emerged in the distributions for the three cohorts (Figure 6), as well as statistically significant differences between the healthy and both pre- and post-CEA cohorts ($p < 0.01$, Figure 6). The exposure to high $RT\bar{\nabla}_{x_{fp}}$ values, quantified by wFPA, resulted significantly different between post-CEA and healthy cohorts only ($p < 0.05$, Figure 6).

For each investigated carotid bifurcation model, the visualization of the surface area exposed to low *TAWSS* (LSA), highlighting wide interindividual variability, is reported in Figure 7. The distribution of the values of *TAWSS* averaged over the bifurcation region in the three cohorts was markedly different between the pre-CEA and both post-CEA and healthy cohorts, as highlighted by the shape of violin plots in Figure 8 and confirmed by the statistically significant differences between the healthy and both pre- and post-CEA cohorts ($p < 0.01$, Figure 8). Statistically significant differences in LSA values in the bifurcation region emerged between the pre-CEA and both post-CEA and healthy cohorts ($p < 0.05$ and $p < 0.01$, respectively, Figure 8), whereas the LSA in the bifurcation region for the post-CEA and healthy cohorts was not significantly different (Figure 8).

Relationships among WSS features

The coefficients of determination R^2 between each couple of WSS-based descriptors are summarized in Table 2. As for the WSS topological skeleton, significant direct associations emerged between wFPA and TSVA for all three cohorts, ranging from $R^2 = 0.463$ ($p < 0.05$) in the post-CEA cohort to $R^2 = 0.646$ ($p < 0.01$) in the pre-CEA cohort (Table 2). For all three cohorts LSA was not associated to either wFPA or TSVA (Table 2), indicating that those WSS topological skeleton descriptors represent statistically independent variables with respect to the commonly adopted exposure to low *TAWSS* as a main indicator of disturbed shear in arteries.^{10,14,26}

Wall shear stress vs. clinical outcome

Linear regressions revealed significant associations between the WSS topological skeleton descriptors and IMT at 60 months follow up. In detail, a significant association emerged between maximum IMT and TSVA ($R^2=0.505$, $p<0.05$) and wFPA ($R^2=0.534$, $p<0.05$), as reported in Table 3. A significant association was observed also between LSA and maximum IMT ($R^2=0.619$, $p<0.001$, Table 3). These associations, albeit slightly weaker ($p<0.05$), were also observed considering the IMT values at the CB (Table 3). In the ICA distally to the CB, wFPA and LSA were significantly associated with the local IMT values (respectively, $R^2=0.541$, $p<0.001$ and $R^2=0.530$, $p<0.05$, Table 3), whereas TSVA was not.

DISCUSSION

WSS topological skeleton features reflect cardiovascular flow complexity,^{3,4,6,24} with direct links to arterial flow patterns like, e.g., near-wall flow stagnation, separation and recirculation, which are known to be promoting factors for cardiovascular disease.^{6,26} In this sense, the role of WSS topological skeleton in vascular pathophysiology is currently based on circumstantial evidence documenting how the complex flow features associated to the WSS topological skeleton induce a focal vascular response.⁶ At the carotid bifurcation, the extent of flow recirculation has been shown to correlate with atherosclerotic biomarkers,²³ while flow stagnation and separation at the carotid bulb have been associated to endothelial dysfunction¹⁴ and intimal thickening,³¹ respectively. In addition, further circumstantial evidence about the role of the WSS topological skeleton in vascular disease has been provided by previous studies demonstrating that the cycle-average WSS topological skeleton governs

the near-wall mass transport in arteries,^{3,6,12} a process linked to the onset and progression of early atherosclerosis.¹¹ Here, we directly link the WSS topological skeleton, within a month after CEA, to vascular response, defined by clinical IMT measurements at 60 months follow-up and an indicator of restenosis, a common adverse event of CEA procedures.²⁷ As a main finding of the study, we report that the investigated WSS topological descriptors TSVA and wFPA were directly associated with the IMT measurements at 60 months follow-up after CEA in the CB and in the ICA (R^2 up to 0.541, $p=0.009$ as presented in Table 3).

Distilling these correlations into mechanistic implications, the here-proposed topological skeleton analysis suggests that exposure to (1) high temporal variation of WSS contraction/expansion action on the endothelium (quantified by TSVA) and (2) high residence times of fixed points at the luminal surface, weighted by WSS contraction/expansion strength (quantified by wFPA), may act as biomechanical triggers of late restenosis after CEA, a process anecdotally anticipated by vascular surgeons to the presence of flow disturbances.²⁷ In other words, our findings support the hypothesis that the WSS topological skeleton features here considered could contribute to promote long-term restenosis, which represents recurrent atherosclerosis.^{18,27} This is corroborated by the fact that, in post-CEA cohort: (1) within 3 months of CEA no sign of lesions (which would represent residual atherosclerosis rather than restenosis²⁷) was reported; (2) short-term restenosis, i.e. beginning 3-6 months postoperatively secondary to neointimal hyperplasia,²⁷ was not clinically observed after 24 months. Therefore, the approach presented here contributes to a deeper understanding of the hemodynamics-driven processes underlying long-term restenosis development in the carotid bifurcation and could be extended to the study of biomechanical triggers of atherosclerosis.

To investigate more in depth the physiological significance of the WSS topological skeleton features, the analysis was extended to a dataset of ostensibly healthy carotid bifurcation models. By comparing the pre-CEA, post-CEA and healthy cohorts, it was possible to understand to what extent the pathological pre-CEA near-wall hemodynamics can be restored towards a more physiological condition as a result of the CEA intervention. Interestingly, it emerged that, on average, CEA interventions were unable to fully restore physiological WSS topological skeleton features of the normal carotid bifurcation (Figures 4 and 6).

On the same post-CEA cohort adopted here, a significant direct association between the exposure to low WSS (quantified by LSA) with maximum IMT at 60 months follow up after CEA was previously reported.¹⁰ An exact understanding of the mechanistic process underlying the development of carotid restenosis after CEA has not yet been achieved; however, the present findings expand the current hypothesis that larger LSAs lead to an increased long-term restenosis risk,¹⁰ by demonstrating that other hemodynamic features besides low shear are independently linked to long-term restenosis. These features are obtained starting from the WSS topological skeleton and quantified by the WSS topological descriptors wFPA and TSVA. The statistical independence between both wFPA and TSVA and LSA in all three examined cohorts (reported in Table 2) suggests that these WSS topological skeleton features and low WSS represent different hemodynamic stimuli, possibly impacting differently the vascular response. Consistently, the co-localization of high $TSVI$ and high $RTV_{x_{fp}}$ regions with low cycle-average WSS regions was moderate for the post-CEA and healthy cohorts, and poor for the pre-CEA cohort (Figures 3, 5 and 7), where a severe stenosis might induce a marked flow recirculation characterized by large variations in the WSS contraction/expansion action, high fixed

points residence time, but concurrently relatively high cycle-average WSS. As a consequence of these observations, in principle the prediction of the long-term restenosis risk by hemodynamic analysis might be improved by taking into account not only the amount of time-averaged low shear,¹⁰ but also the introduced descriptors based on WSS topological skeleton. As previously reported on the same post-CEA cohort adopted here,¹⁰ the exposure to oscillatory WSS was not associated to IMT, thereby suggesting differences in the vascular response to focal (i.e., point-based) WSS oscillatory directional changes with respect to directional changes in the neighborhood of a point leading to variations in the contraction/expansion action.

On the other hand, although the different physical meanings underpinning the two WSS topological skeleton descriptors wFPA and TSVA (i.e., exposure to non-null values of the residence time of a fixed point, weighted by the local WSS contraction/expansion action vs. exposure to high normalized WSS divergence variability, respectively), a significant association between them emerged in all three cohorts (Table 2). This was consistent with the observed co-localization between luminal surface areas exposed to high $TSVI$ and $RT\bar{V}_{x_{fp}}$ in all models (Figures 3 and 5, respectively), with the former encompassing the latter. Consequently, fixed points occurred in regions where normalized WSS divergence variations were high (Figure 3) and the contraction/expansion regions connecting fixed points was characterized by both high normalized WSS divergence absolute values and high normalized WSS divergence variations (Figure 3).

At 60 months, restenosis occurred in post-CEA carotid models PG1 and PG2, with diameter stenosis >70% and >50% respectively.¹⁰ Notably, in the post-CEA cohort, PG1 was characterized by the highest wFPA value, while PG2 had the highest TSVA value (Figures 3 and 5). Those two cases were also

characterized by the highest LSA values in the post-CEA cohort, as can be seen in Figure 7 and as previously reported,¹⁰ although using a different *TAWSS* threshold value to define LSA. A marked intima-media thickening was also observed¹⁰ at 60 months follow-up in post-CEA patients PG3 and PC2 at the FD, PG6 in the CCA (FD-2cm), in correspondence of either low cycle-average WSS (PG3, Figure 7) or large variations in the WSS contraction/expansion and weighted fixed point residence times (Figures 3 and 5, respectively).

This study faces possible limitations. Among them, we mention differences between the CEA patients and healthy cohorts, mainly in terms of cohort size and mean age (72.8 ± 7.2 vs. 58.7 ± 11.8 , respectively). These differences can be partially ascribed to the clinical real-world nature of the data adopted for the CEA cohorts, which however allowed to address the typical challenges related to longitudinal studies (e.g., long time-scale of the vascular pathophysiology processes, patients' recruitment and follow-up). Moreover, randomization was not performed for the selection of the CEA patients, and the exact extension of the region that underwent CEA surgical intervention (either with or without graft) could not be extracted from the imaging data. The relationships here reported might be influenced by the uncertainties (e.g., reconstruction errors) and assumptions/idealizations (e.g., Newtonian viscosity, rigid walls, as widely discussed elsewhere^{20,30}) affecting computational hemodynamics. Because of these limitations, future investigations are warranted to further confirm the validity of the relationships presented here.

CONCLUSIONS

Our study confirms what previous studies^{4,6,24} on the WSS topological skeleton have only been able to infer: WSS topological skeleton features are directly associated to the vascular response. High variability in the WSS contraction/expansion and high WSS fixed points weighted residence times were directly associated to markers of vascular disease at the carotid bifurcation. Moreover, the findings of this study may help in clarifying the role played by hemodynamics in the mechanisms underlying the development of long-term carotid restenosis after CEA (and, by extension, of atherosclerosis), demonstrating that WSS topological skeleton features might represent a different hemodynamic cue with respect to low WSS. Nevertheless, further investigations detailing and elucidating the effects of the WSS topological skeleton on vascular pathophysiology are encouraged. In this regard, the here applied Eulerian-based method for topological skeleton analysis²⁴ confirms its potential as an effective biomechanical tool for increasing the chance of elucidating the existing mechanistic link between flow disturbances and clinical observations.

ACKNOWLEDGEMENTS

CV has been partially supported by the H2020-MSCA-ITN-2017, EU project 765374 "ROMSOC - Reduced Order Modelling, Simulation and Optimization of Coupled systems" and by the Italian research project MIUR PRIN17 2017AXL54F "Modeling the heart across the scales: from cardiac cells to the whole organ".

REFERENCES

1. AbuRahma, A. F., P. Stone, S. Deem, L. S. Dean, T. Keiffer, and E. Deem. Proposed duplex velocity criteria for carotid restenosis following carotid endarterectomy with patch closure. *J. Vasc. Surg.* , 2009.doi:10.1016/j.jvs.2009.01.065
2. Antiga, L., M. Piccinelli, L. Botti, B. Ene-Iordache, A. Remuzzi, and D. A. Steinman. An image-based modeling framework for patient-specific computational hemodynamics. *Med. Biol. Eng. Comput.* 46:1097–1112, 2008.
3. Arzani, A., A. M. Gambaruto, G. Chen, and S. C. Shadden. Lagrangian wall shear stress structures and near-wall transport in high-Schmidt-number aneurysmal flows. *J. Fluid Mech.* , 2016.doi:10.1017/jfm.2016.6
4. Arzani, A., A. M. Gambaruto, G. Chen, and S. C. Shadden. Wall shear stress exposure time: a Lagrangian measure of near-wall stagnation and concentration in cardiovascular flows. *Biomech. Model. Mechanobiol.* , 2017.doi:10.1007/s10237-016-0853-7
5. Arzani, A., and S. C. Shadden. Characterizations and Correlations of Wall Shear Stress in Aneurysmal Flow. *J. Biomech. Eng.* , 2016.doi:10.1115/1.4032056
6. Arzani, A., and S. C. Shadden. Wall shear stress fixed points in cardiovascular fluid mechanics. *J. Biomech.* , 2018.doi:10.1016/j.jbiomech.2018.03.034
7. Bijari, P. B., L. Antiga, D. Gallo, B. A. Wasserman, and D. A. Steinman. Improved prediction of disturbed flow via hemodynamically-inspired geometric variables. *J. Biomech.* 45:1632–1637, 2012.
8. Domanin, M., D. Bissacco, D. Le Van, and C. Vergara. Computational fluid dynamic comparison between patch-based and primary closure techniques after carotid endarterectomy. *J. Vasc. Surg.* , 2018.doi:10.1016/j.jvs.2017.08.094
9. Domanin, M., A. Buora, F. Scardulla, B. Guerciotti, L. Forzenigo, P. Biondetti, and C. Vergara. Computational Fluid-Dynamic Analysis after Carotid Endarterectomy: Patch Graft versus Direct Suture Closure. *Ann. Vasc. Surg.* , 2017.doi:10.1016/j.avsg.2017.04.016
10. Domanin, M., D. Gallo, C. Vergara, P. Biondetti, L. V. Forzenigo, and U. Morbiducci. Prediction of Long Term Restenosis Risk After Surgery in the Carotid Bifurcation by Hemodynamic and Geometric Analysis. *Ann. Biomed. Eng.* , 2019.doi:10.1007/s10439-019-02201-8
11. Ethier, C. R. Computational modeling of mass transfer and links to atherosclerosis. *Ann. Biomed. Eng.* , 2002.doi:10.1114/1.1468890
12. Farghadan, A., and A. Arzani. The combined effect of wall shear stress topology and magnitude on cardiovascular mass transport. *Int. J. Heat Mass Transf.* , 2019.doi:10.1016/j.ijheatmasstransfer.2018.11.051
13. Frericks, H., J. Kievit, J. M. Van Baalen, and J. H. Van Bockel. Carotid recurrent stenosis and risk of ipsilateral stroke: A systematic review of the literature. *Stroke* ,

1998.doi:10.1161/01.STR.29.1.244

14. Gallo, D., P. B. Bijari, U. Morbiducci, Y. Qiao, Y. J. Xie, M. Etesami, D. Habets, E. G. Lakatta, B. A. Wasserman, and D. A. Steinman. Segment-specific associations between local haemodynamic and imaging markers of early atherosclerosis at the carotid artery: an in vivo human study. *J. R. Soc. Interface* 15:, 2018.
15. Gallo, D., D. A. Steinman, and U. Morbiducci. Insights into the co-localization of magnitude-based versus direction-based indicators of disturbed shear at the carotid bifurcation. *J. Biomech.* , 2016.doi:10.1016/j.jbiomech.2016.02.010
16. Gambaruto, A. M., and A. J. João. Flow structures in cerebral aneurysms. *Comput. Fluids* , 2012.doi:10.1016/j.compfluid.2012.02.020
17. Guerciotti, B., C. Vergara, L. Azzimonti, L. Forzenigo, A. Buora, P. Biondetti, and M. Domanin. Computational study of the fluid-dynamics in carotids before and after endarterectomy. *J. Biomech.* , 2016.doi:10.1016/j.jbiomech.2015.11.009
18. Hellings, W. E., F. L. Moll, J. P. P. M. De Vries, P. De Bruin, D. P. V. De Kleijn, and G. Pasterkamp. Histological characterization of restenotic carotid plaques in relation to recurrence interval and clinical presentation: A cohort study. *Stroke* , 2008.doi:10.1161/STROKEAHA.107.496703
19. Ku, D. N., D. P. Giddens, C. K. Zarins, and S. Glagov. Pulsatile flow and atherosclerosis in the human carotid bifurcation. Positive correlation between plaque location and low and oscillating shear stress. *Arteriosclerosis* , 1985.doi:10.1161/01.atv.5.3.293
20. Lancellotti, R. M., C. Vergara, L. Valdetaro, S. Bose, and A. Quarteroni. Large eddy simulations for blood dynamics in realistic stenotic carotids. *Int. j. numer. method. biomed. eng.* , 2017.doi:10.1002/cnm.2868
21. Lee, S. W., L. Antiga, J. D. Spence, and D. A. Steinman. Geometry of the carotid bifurcation predicts its exposure to disturbed flow. *Stroke* , 2008.doi:10.1161/STROKEAHA.107.510644
22. Lee, S. W., and D. A. Steinman. On the relative importance of rheology for image-based CFD models of the carotid bifurcation. *J. Biomech. Eng.* , 2007.doi:10.1115/1.2540836
23. Martorell, J., P. Santomá, K. Kolandaivelu, V. B. Kolachalama, P. Melgar-Lesmes, J. J. Molins, L. Garcia, E. R. Edelman, and M. Balcells. Extent of flow recirculation governs expression of atherosclerotic and thrombotic biomarkers in arterial bifurcations. *Cardiovasc. Res.* , 2014.doi:10.1093/cvr/cvu124
24. Mazzi, V., D. Gallo, K. Calò, M. Najafi, M. O. Khan, G. De Nisco, D. A. Steinman, and U. Morbiducci. A Eulerian method to analyze wall shear stress fixed points and manifolds in cardiovascular flows. *Biomech. Model. Mechanobiol.* , 2019.doi:10.1007/s10237-019-01278-3
25. Morbiducci, U., D. Gallo, D. Massai, R. Ponzini, M. A. Deriu, L. Antiga, A. Redaelli, and F. M. Montevecchi. On the importance of blood rheology for bulk flow in hemodynamic models of the carotid bifurcation. *J. Biomech.* , 2011.doi:10.1016/j.jbiomech.2011.06.028

26. Morbiducci, U., A. M. Kok, B. R. Kwak, P. H. Stone, D. A. Steinman, and J. J. Wentzel. Atherosclerosis at arterial bifurcations: Evidence for the role of haemodynamics and geometry. *Thromb. Haemost.* , 2016.doi:10.1160/TH15-07-0597
27. Naylor, A. R. *et al.* Editor's Choice – Management of Atherosclerotic Carotid and Vertebral Artery Disease: 2017 Clinical Practice Guidelines of the European Society for Vascular Surgery (ESVS). *Eur. J. Vasc. Endovasc. Surg.* , 2018.doi:10.1016/j.ejvs.2017.06.021
28. Peiffer, V., S. J. Sherwin, and P. D. Weinberg. Does low and oscillatory wall shear stress correlate spatially with early atherosclerosis? A systematic review. , 2013.doi:10.1093/cvr/cvt044
29. Steinman, D. A., J. B. Thomas, H. M. Ladak, J. S. Milner, B. K. Rutt, and J. David Spence. Reconstruction of carotid bifurcation hemodynamics and wall thickness using computational fluid dynamics and MRI. *Magn. Reson. Med.* , 2002.doi:10.1002/mrm.10025
30. Taylor, C. A., and D. A. Steinman. Image-Based Modeling of Blood Flow and Vessel Wall Dynamics: Applications, Methods and Future Directions. *Ann. Biomed. Eng.* , 2010.doi:10.1007/s10439-010-9901-0
31. Zarins, C. K., D. P. Giddens, B. K. Bharadvaj, V. S. Sottiurai, R. F. Mabon, and S. Glagov. Carotid bifurcation atherosclerosis. Quantitative correlation of plaque localization with flow velocity profiles and wall shear stress. *Circ. Res.* 53:502–514, 1983.

FIGURE LEGENDS

FIGURE 1 Explanatory sketch of the topological skeleton of a vector field. Configuration of each fixed point-type and contraction/expansion regions, colored in blue/red respectively, are displayed. The Poincarè index (used for fixed points identification) and the eigenvalues of the Jacobian matrix (used for fixed points classification²⁴) associated with each fixed point type are reported.

FIGURE 2 Topological skeleton of cycle-average WSS vector in pre-CEA, post-CEA and healthy cohorts. The topological skeleton in pre-CEA and post-CEA cohorts is extended beyond the bifurcation region (delimited by sections CCA3-ICA5-ECA2) to include in the pre-CEA models possible distal ICA/ECA stenoses. Blue and red color define contraction and expansion regions, respectively. The WSS vector field is normalized for visualization.

FIGURE 3 Luminal distribution of $TSVI$ in pre-CEA, post-CEA and healthy cohorts. The $TSVI$ distribution in pre-CEA and post-CEA cohorts is extended beyond the bifurcation region (delimited by sections CCA3-ICA5-ECA2) to include in the pre-CEA models possible distal ICA/ECA stenoses. The 80th percentile value of the pooled $TSVI$ distribution of the healthy cohort in the bifurcation region is reported in the legend.

FIGURE 4 Violin plots of the mean value of $TSVI$ and TSVA in the bifurcation region (delimited by sections CCA3-ICA5-ECA2) for pre-CEA, post-CEA and healthy cohorts. The distribution, median and quartile range are displayed for each cohort. Differences among the three cohorts are evaluated with a Wilcoxon signed-rank test.

FIGURE 5 Luminal distribution of WSS fixed points weighted residence time ($RT\bar{V}_{x_{fp}}$) in pre-CEA, post-CEA and healthy cohorts. The $RT\bar{V}_{x_{fp}}$ distribution in pre-CEA and post-CEA cohorts is extended beyond

the bifurcation region (delimited by sections CCA3-ICA5-ECA2) to include in the pre-CEA models possible distal ICA/ECA stenoses.

FIGURE 6 Violin plots of the mean value of $RT\bar{\nabla}_{x_{fp}}$ and wFPA in the bifurcation region (delimited by sections CCA3-ICA5-ECA2) for pre-CEA, post-CEA and healthy cohorts. Distribution, median and quartile range are displayed for each cohort. Differences among the three cohorts are evaluated with a Wilcoxon signed-rank test.

FIGURE 7 Luminal surface area exposed to low TAWSS as expressed by LSA, in pre-CEA, post-CEA and healthy cohorts. The LSA in pre-CEA and post-CEA cohorts is extended beyond the bifurcation region (delimited by sections CCA3-ICA5-ECA2) to include in the pre-CEA models possible distal ICA/ECA stenoses. Red areas represent TAWSS value below the 20th percentile of the pooled TAWSS distribution of the healthy models in the bifurcation region.

FIGURE 8 Violin plots of the mean value of TAWSS and LSA in the bifurcation region (delimited by sections CCA3-ICA5-ECA2) for pre-CEA, post-CEA and healthy cohorts. Distribution, median and quartile range are displayed for each cohort. Differences among the three cohorts are evaluated with a Wilcoxon signed-rank test.

TABLES

Table 1. Patient data.

Patient	Age (years)	Sex	Clinical Risk Factors	Stenosis Location	ICA ϕ (mm)
PG1*	65	F	HTN	CCA, CB	5.00
PG2*	65	F	HTN	CB	5.40
PG3	81	F	HTN, SMOKE	CB, ICA	4.20
PG4	82	F	HTN	CB, ICA	4.00
PG5	72	M	HTN, DIAB, SMOKE	ICA	4.50
PG6	68	F	HTN, SMOKE	CB	4.50
PG7	71	F	HTN	CB, ICA	4.90
PG8	76	M	HTN, SMOKE	CB	4.00
PG9	67	M	HTN, DIAB, DYSLIP, SMOKE	CB, ICA	4.80
PC1	81	F	HTN, DYSLIP, SMOKE	CB, ICA	4.74
PC2	79	M	DIAB, DYSLIP	CB, ICA	5.00
PC3	79	M	HTN, DIAB, DYSLIP, SMOKE	CCA, CB, ICA	7.00
PC4	61	M	HTN, DYSLIP	CB	6.60

Age, classification of sex (F female; M male), clinical risk factors (HTN: presence of hypertension, DIAB: diabetes, DYSLIP: dyslipidemia, SMOKE: smoking), location of the carotid stenosis (CCA Common carotid artery; CB Carotid bulb; ICA Internal carotid artery; ECA external carotid artery), peak systolic velocity (PSV) measurements at the stenosis, and diameter measurements at CCA, CB, ICA and ECA.

* Cases PG1 and PG2: respectively, right and left carotid of the same patient.

Table 2. Pairwise correlations among the relative exposure to high *TSVI* (TSVA), non-null $RT\bar{V}_{x_{fp}}$ (wFPA) and low *TAWSS* (LSA).

Coefficient of Determination R^2	PRE		POST		HEALTHY	
	TSVA	LSA	TSVA	LSA	TSVA	LSA
wFPA	0.646‡	0.075	0.463‡	0.292	0.554‡	0.001
TSVA	-	0.193	-	0.164	-	0.011

* $p < 0.05$; † $p < 0.01$; ‡ $p < 0.001$

Table 3. Relationship between the hemodynamic variables TSVA, wFPA or LSA and IMT measurements.

Coefficient of Determination R^2	TSVA	wFPA	LSA
Maximum IMT	0.505*	0.534*	0.619‡
IMT @ FD-2cm	0.116	0.108	0.006
IMT @ FD-1cm	0.004	0.271	0.046
IMT @ FD	0.032	0.161	0.272
IMT @ CB	0.474*	0.425*	0.421*
IMT @ ICA	0.090	0.541†	0.530*

* $p < 0.05$; † $p < 0.01$; ‡ $p < 0.001$

IMT Intima-media thickness, CCA common carotid artery, CB carotid bulb, FD flow divider, ICA internal carotid artery. Maximum IMT, IMT measured at the bifurcation level (flow divider FD), CCA at 2cm and 1cm proximal to the FD (FD-2cm and FD-1cm), at the CB, at the ICA downstream of the CB.

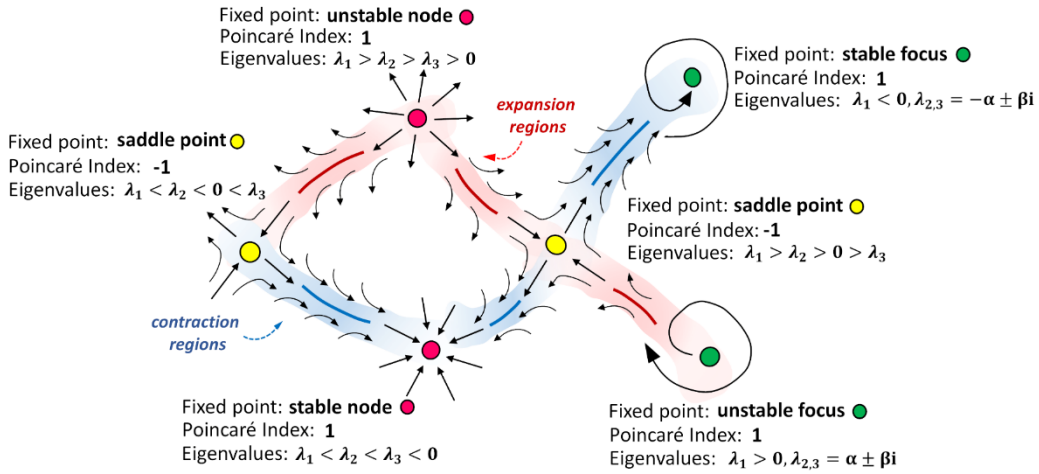


FIGURE 1.

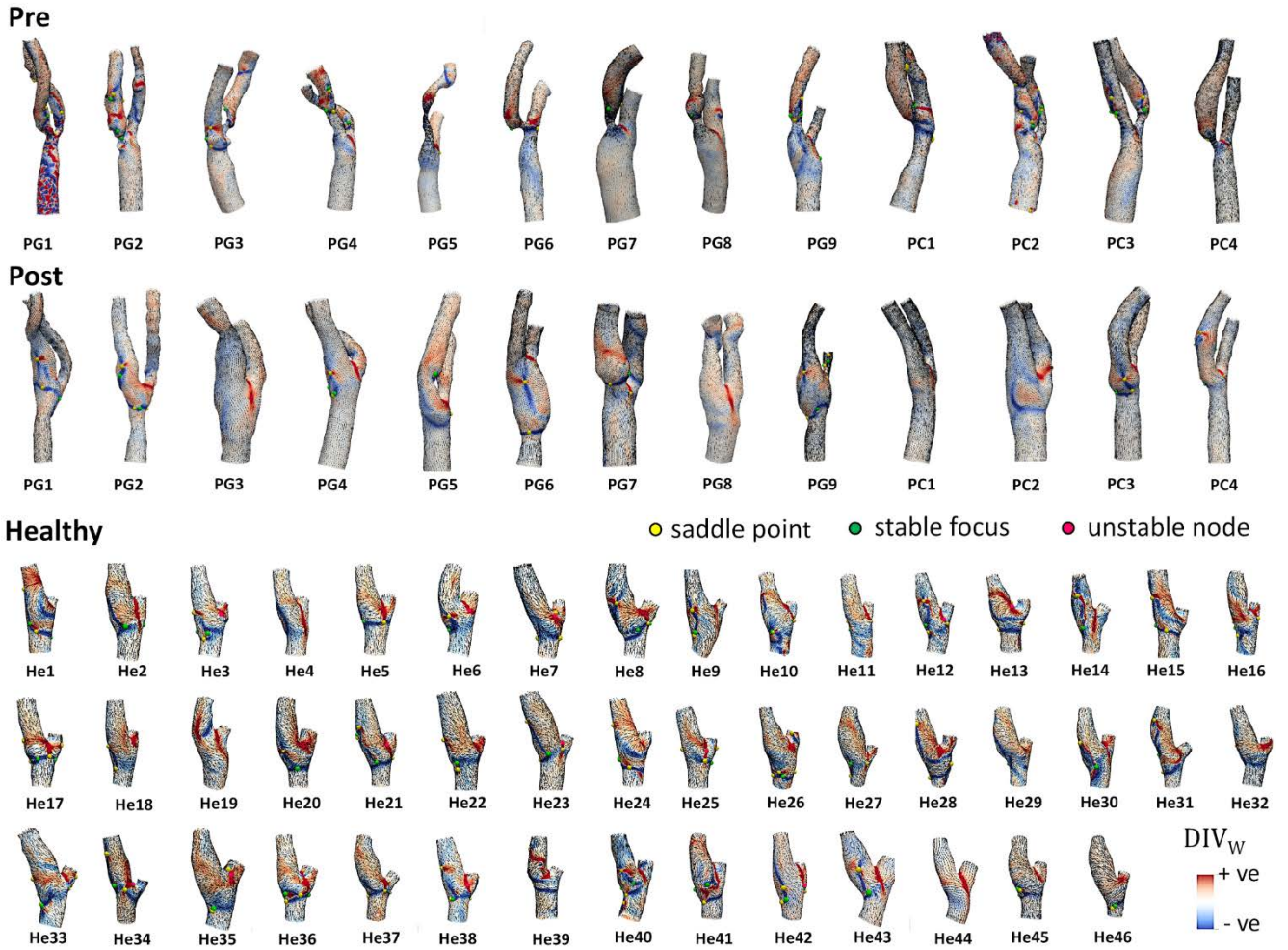


FIGURE 2.

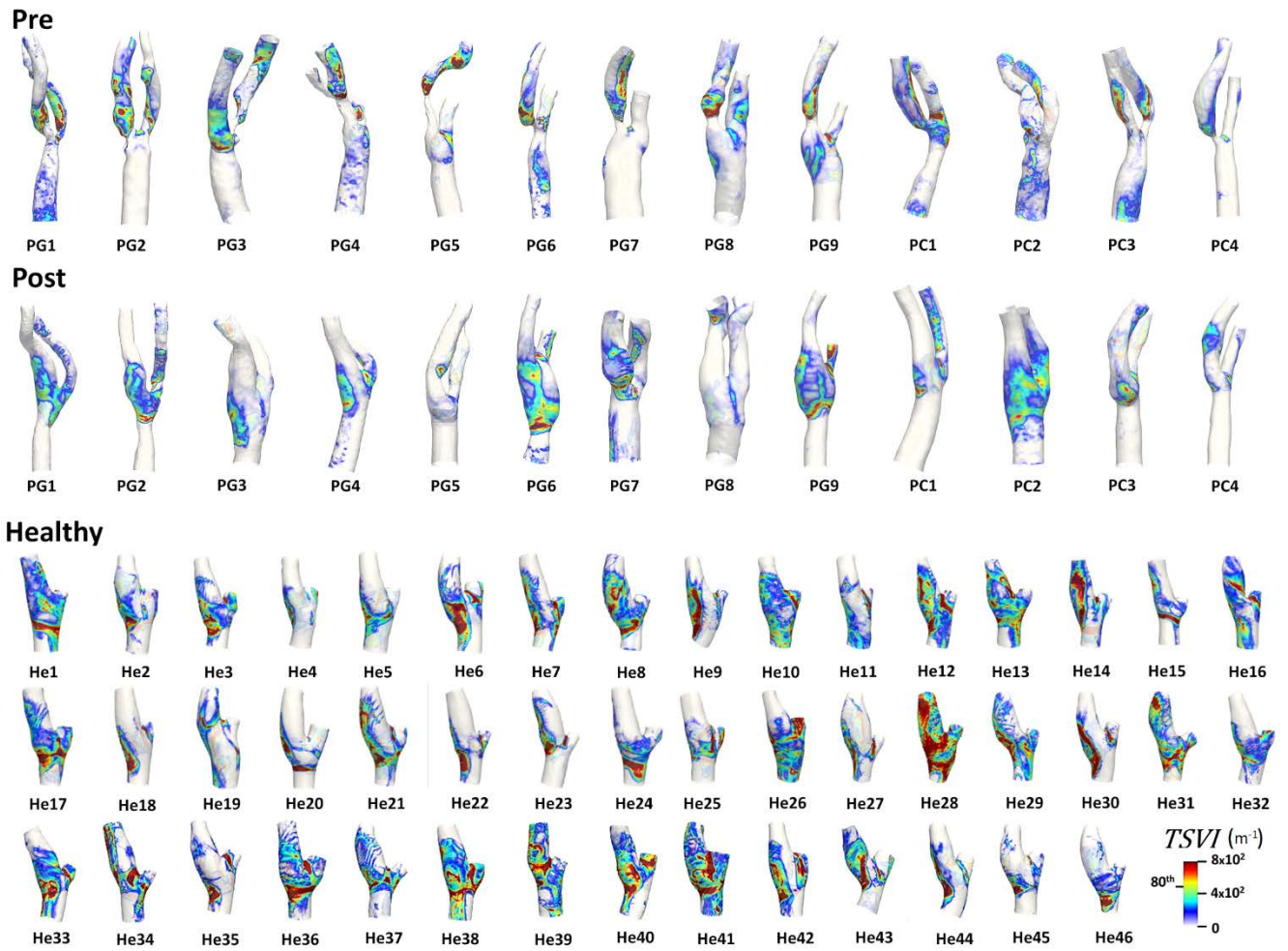


FIGURE 3.

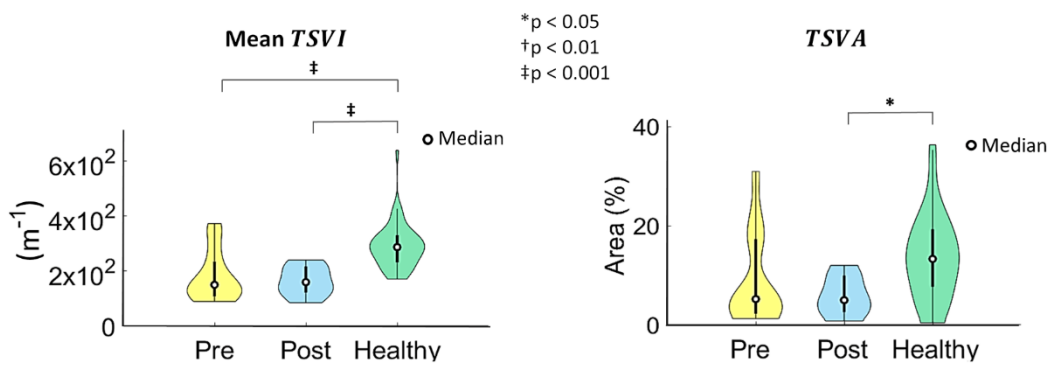
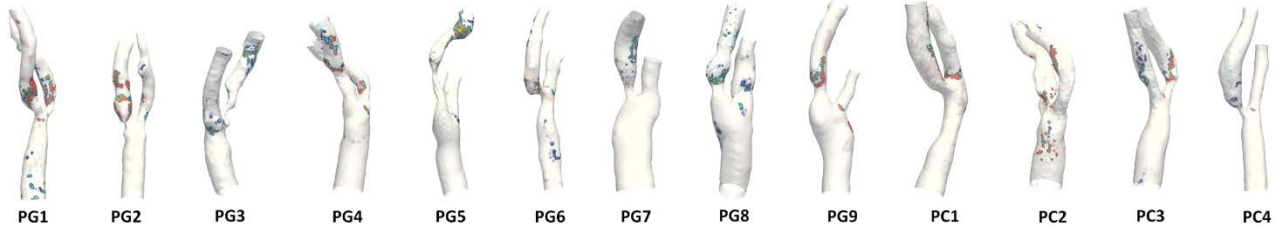
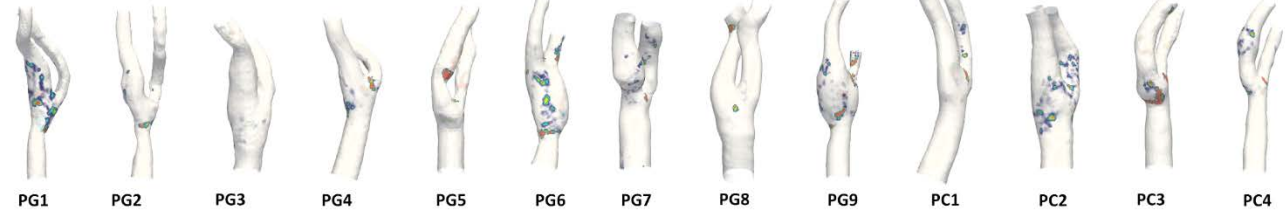


FIGURE 4.

Pre



Post



Healthy

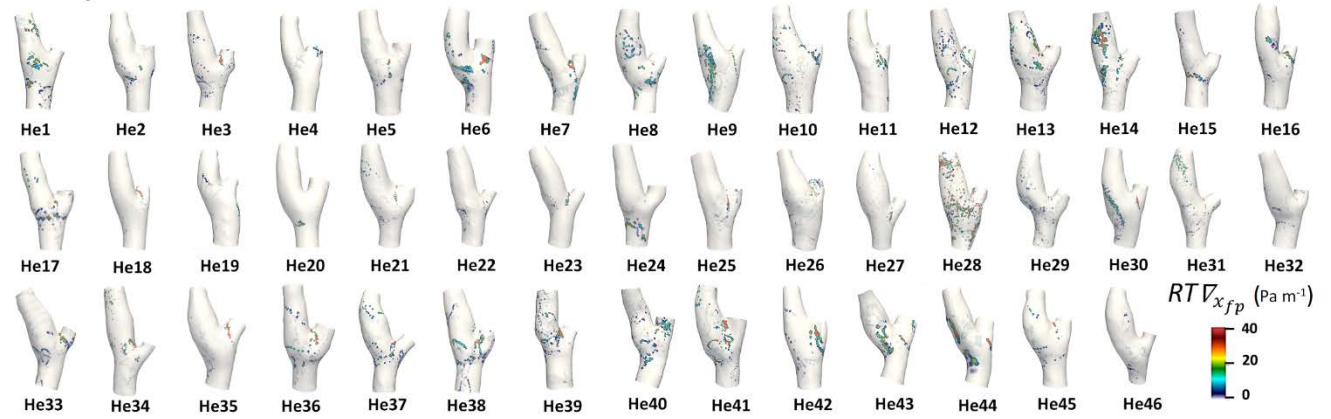


FIGURE 5.

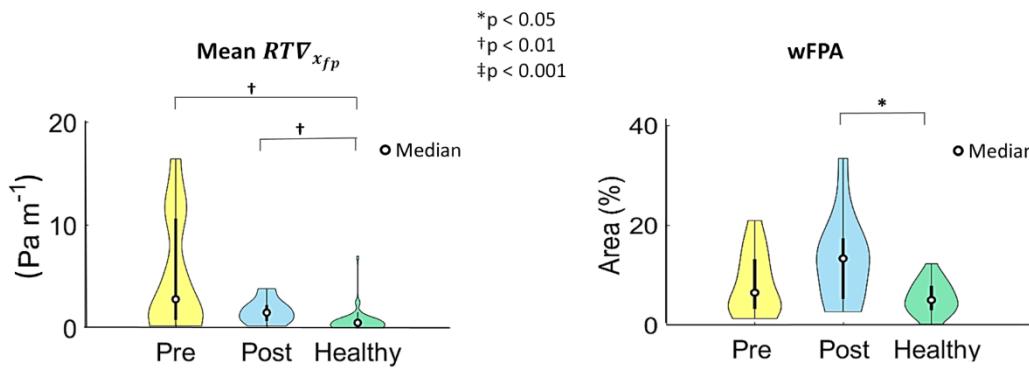
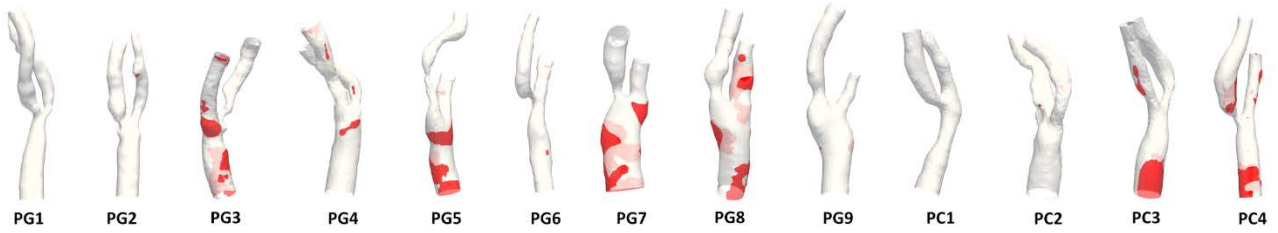
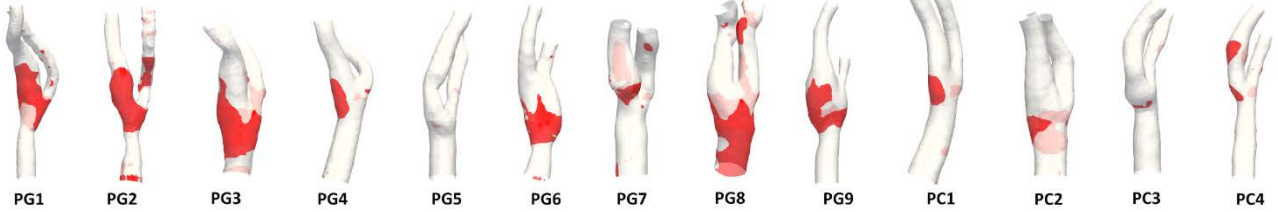


FIGURE 6.

Pre



Post



Healthy

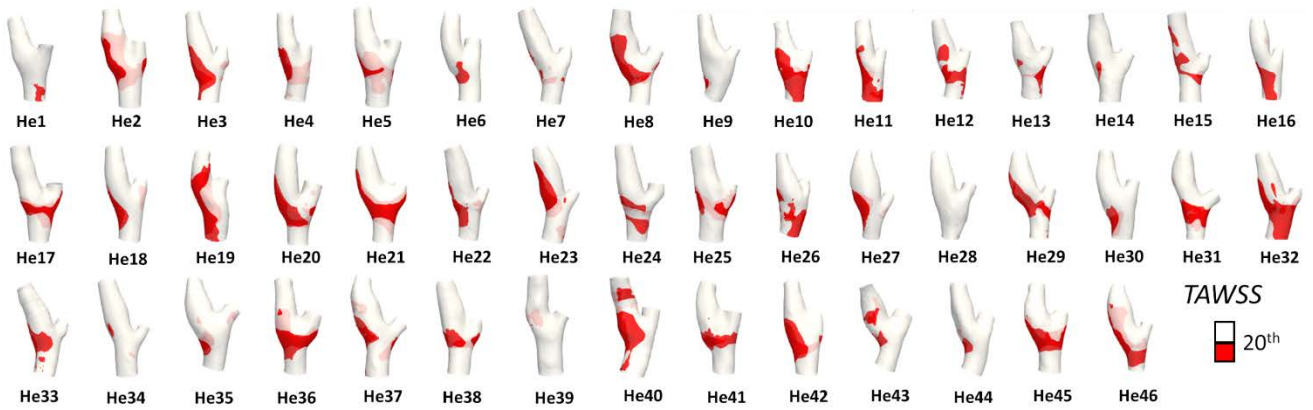


FIGURE 7.

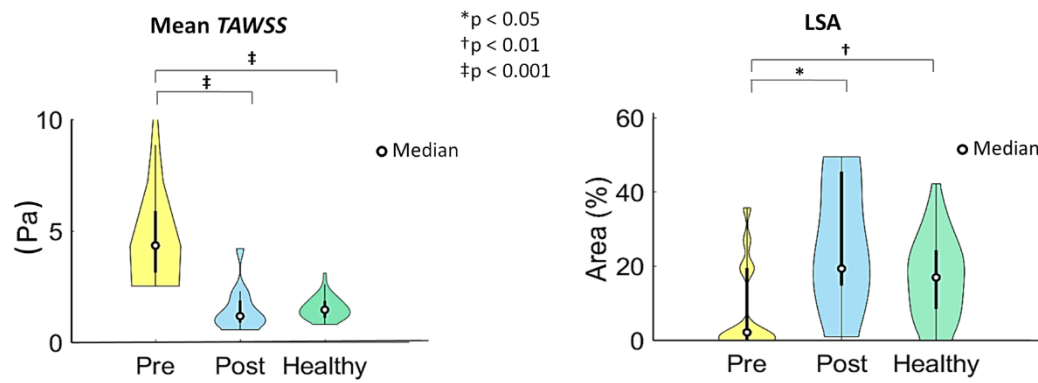


FIGURE 8.

MOX Technical Reports, last issues

Dipartimento di Matematica
Politecnico di Milano, Via Bonardi 9 - 20133 Milano (Italy)

- 34/2020** Antonietti, P.F.; Mazziere, I.; Nati Poltri, S.
A high-order discontinuous Galerkin method for the poro-elasto-acoustic problem on polygonal and polyhedral grids
- 33/2020** Centofanti, F.; Fontana, M.; Lepore, A.; Vantini, S.
Smooth LASSO Estimator for the Function-on-Function Linear Regression Model
- 32/2020** Menafoglio, A.; Sgobba, S.; Lanzano, G.; Pacor, F.
Simulation of seismic ground motion fields via object-oriented spatial statistics: a case study in Northern Italy
- 31/2020** Bernardi, M.S.; Africa, P.C.; de Falco, C.; Formaggia, L.; Menafoglio, A.; Vantini, S.
On the Use of Interferometric Synthetic Aperture Radar Data for Monitoring and Forecasting Natural Hazards
- 30/2020** Massi, M.C., Gasperoni, F., Ieva, F., Paganoni, A.M., Zunino, P., Manzoni, A., Franco, N.R., e
A deep learning approach validates genetic risk factors for late toxicity after prostate cancer radiotherapy in a REQUITE multinational cohort
- 29/2020** Piersanti, R.; Africa, P.C.; Fedele, M.; Vergara, C.; Dede', L.; Corno, A.F.; Quarteroni, A.
Modeling cardiac muscle fibers in ventricular and atrial electrophysiology simulations
- 26/2020** Zonca, S.; Antonietti, P.F.; Vergara, C.
A Polygonal Discontinuous Galerkin formulation for contact mechanics in fluid-structure interaction problems
- 28/2020** Regazzoni, F.; Dedè, L.; Quarteroni, A.
Biophysically detailed mathematical models of multiscale cardiac active mechanics
- 27/2020** Spreafico, M.; Ieva, F.; Fiocco, M.
Modelling dynamic covariates effect on survival via Functional Data Analysis: application to the MRC BO06 trial in osteosarcoma
- Regazzoni, F.; Dedè, L.; Quarteroni, A.
Biophysically detailed mathematical models of multiscale cardiac active mechanics